This article has been accepted for publication in a future issue of this journal, but has not been fully edited. Content may change prior to final publication. Citation information: DOI 10.1109/JLT.2014.2310780, Journal of Lightwave Technology

40 GHz Si/Ge uni-traveling carrier waveguide photodiode

Molly Piels and John E. Bowers, *Fellow, IEEE*

***Abstract*—We report a Si/Ge waveguide-coupled uni-traveling carrier (UTC) photodiode for high-power high-speed applications. Using the uni-traveling carrier structure rather than a PIN structure, capacitance and power handling are decoupled from responsivity and transit-time, enabling a detector with a 40 GHz bandwidth and a dilute absorption profile. This photodiode had a responsivity at 1550 nm of 0.5 A/W and a -1 dB compression current of 1.5 mA at 40 GHz. A longer device with the same cross-section had a 33 GHz bandwidth, responsivity of 0.7 A/W, and -1 dB compression current of 2.1 mA at 30 GHz.**

***Index Terms*—microwave photonics, photodetectors, silicon photonics, uni-traveling-carrier photodiode**

I. Introduction

Microwave photonic links require photodiodes with large bandwidth, high efficiency, and large saturated output power. The silicon/germanium system is appealing for microwave photonics applications due to the high thermal conductivities of silicon and germanium relative to InP and InGaAs, the durability and low cost of the substrate material, and high-speed and high-power performance of demonstrated devices [1]-[5].

There are numerous design trade-offs between speed, efficiency, and output power. For germanium-based photodiodes, even at relatively low operating frequencies, waveguide-based designs are often more promising than surface-normal designs because the bandwidth-efficiency product of germanium is only 10 GHz [6],[7]. For high-power waveguide photodiodes, dilute absorption profiles are preferable to abrupt ones because the current can be more evenly distributed over the entire device area [8],[9], but require devices to be longer in order to achieve good efficiency. This can come at a cost of increased diode capacitance and corresponding reduced bandwidth.

In the Si/Ge material system, a uni-traveling carrier (UTC) design can be used to decrease the capacitance per unit area relative to a PIN detector [10]. This allows high-efficiency detectors with dilute absorption profiles to be designed. Unlike metal-semiconductor-metal designs, which can also have reduced capacitance per unit area relative to PIN detectors, the UTC has a high breakdown voltage, which is beneficial for high-power performance. Here, we demonstrate two waveguide coupled Si/Ge UTC photodiodes with dilute absorption profiles. One had a 3 dB bandwidth of 40 GHz, responsivity at 1550 nm of 0.5 A/W, and a -1dB compression current at 40 GHz of 1.5 mA. A longer detector had a 3 dB bandwidth of 33 GHz, responsivity at 1550 nm of 0.7 A/W, and a -1dB compression current at 30 GHz of 2.1 mA.

This work was supported by the DARPA MTO EPHI project.

M. Piels was with the University of California, Santa Barbara. She is now with the Department of Photonic Engineering, Technical University of Denmark, DK-2800 Kgs. Lyngby, Denmark (phone: +45 45 25 51 82; fax: +45 45 93 65 81 e-mail: mopi@fotonik.dtu.dk).

J. E. Bowers is with the Department of Electrical and Computer Engineering, University of California, Santa Barbara, 93106 (phone: 805-893-8447; fax: 805-893-7990; e-mail: bowers@ece.ucsb.edu).

II. Design

Fig.s 1 (a) and (b) show the band diagram and doping profile of a Si/Ge uni-traveling carrier photodiode. The germanium is entirely p-doped, while the intrinsic region and n-sides of the diode are in the silicon. Thus the diode capacitance and breakdown voltage are determined by the silicon collector thickness rather than the germanium thickness.

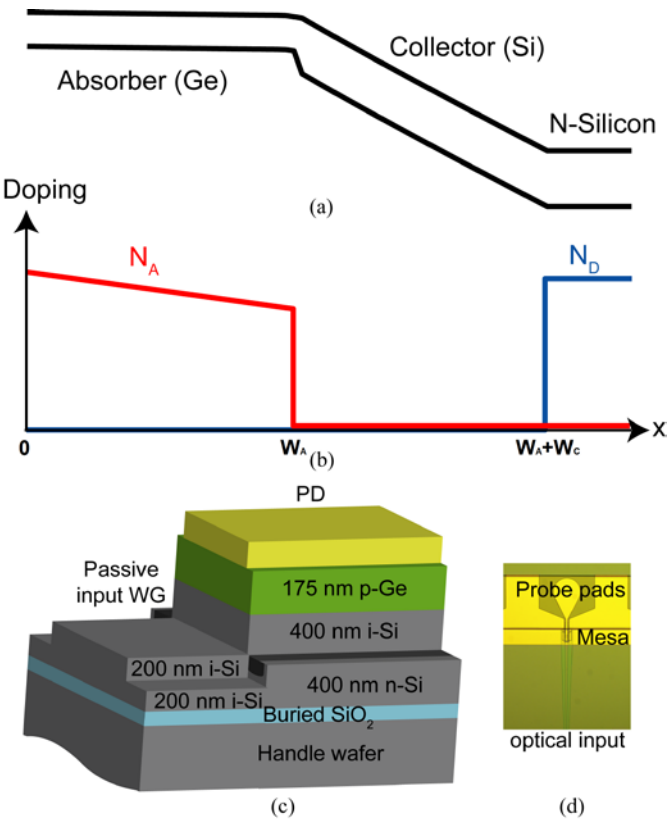

Fig. 1. (a) Band diagram and (b) doping profile of a Si/Ge UTC photodiode and coordinate system definition for (1)-(5). (c) Schematic and (d) micrograph of a fabricated device.

This article has been accepted for publication in a future issue of this journal, but has not been fully edited. Content may change prior to final publication. Citation information: DOI 10.1109/JLT.2014.2310780, Journal of Lightwave Technology

A cross-section schematic of the device is shown in Fig. 1 (c). The absorber thickness of 175 nm was chosen to maximize quantum efficiency. In general, the quantum efficiency of a Si/Ge UTC is limited by both the absorption profile (and length) and the collection efficiency, or the number of photogenerated electrons that contribute to current in the external circuit. Fig. 2 shows the simulated quantum efficiency of a 20 μm long device at 1550 nm as a function of germanium thickness. The effects of the absorption profile and limited collection efficiency are shown independently in the figure. The optical simulation was done using the beam propagation method for an input of the fundamental TE mode of the silicon rib waveguide and assuming a perfectly conducting top contact. Other simulation parameters are given in Table 1. Optically, there are optimum points around 200, 500, and 800 nm that correspond to strong coupling from the input passive waveguide to the absorption region. Choosing an absorber thickness near one of these points enables short, low-capacitance devices with good responsivity.

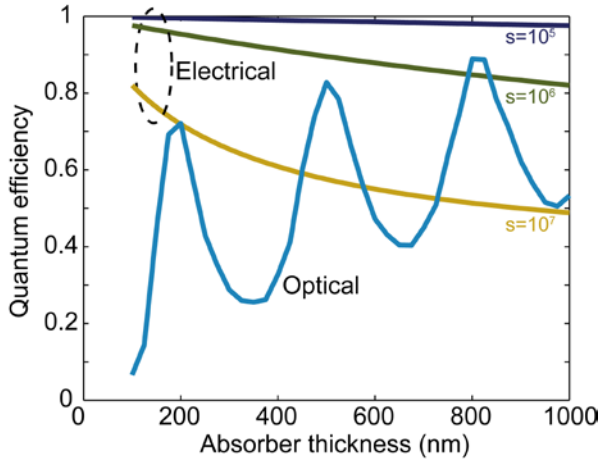

Fig. 2. Simulated photodiode efficiency as a function of absorber thickness. The optical simulation was done using the beam propagation method and the input was the fundamental TE mode of the passive silicon waveguide. The electrical curves were generated using (2)-(4), and the collection efficiency is defined in (5). All simulation parameters can be found in Table 1. The collection efficiency is similar for all $s \le 10^5$ cm/s.

To estimate the collection efficiency of the device, we solved the drift-diffusion equations for a one-dimensional photodiode using the same approach as Ishibashi et al. [11]. Since no diffusion-blocking layer was used for these diodes (a diffusion-blocking layer would have improved their performance, but is difficult to grow), some of the photogenerated electrons will diffuse into p-contact, decreasing the quantum efficiency of the device. To account for this, the boundary condition at the p-contact had to be adjusted. Instead of assuming zero electron current, we use

$$J_n(0) = qn(0)s \tag{1}$$

where s is the back-surface recombination velocity, and is at most the thermal velocity of electrons in germanium ($1\cdot10^7$ cm/s). The boundary condition at the other end of the absorber is similar; $J_n(W_A) = qn(W_A)v_e$, where v_e is the electron velocity at the absorber-collector junction. The coordinate system is as defined in Fig. 1 (b). This yields the following expression for the electron current in the absorber:

$$\frac{1}{q}J_n(x) = (v_d + D_n m_1)C_1 e^{m_1 x} + (v_d + D_n m_2)C_2 e^{m_2 x}, \tag{2}$$

where q is the electron charge, v_d is the drift velocity in the absorber ($\mu_n E$, assumed constant), D_n is the diffusion coefficient, m_1 and m_2 are as defined in [11],

$$m_1 = -\frac{v_d}{2D_n} - \sqrt{\left(\frac{v_d}{2D_n}\right)^2 + \frac{1+j\omega\tau}{D_n\tau}}, \tag{3a}$$

$$m_2 = -\frac{v_d}{2D_n} + \sqrt{\left(\frac{v_d}{2D_n}\right)^2 + \frac{1+j\omega\tau}{D_n\tau}}, \tag{3b}$$

$$C_1 = \frac{1}{|\Delta|}\frac{G\tau}{1+j\omega\tau}\begin{vmatrix} (v_d - s)e^{m_2 W_A} & v_d + v_e \\ v_d + D_n m_2 - s & v_d + D_n m_2 + v_e \end{vmatrix}, \tag{3c}$$

$$C_2 = \frac{1}{|\Delta|}\frac{G\tau}{1+j\omega\tau}\begin{vmatrix} v_d + v_e & (v_d - s)e^{m_1 W_A} \\ v_d + D_n m_1 + v_e & v_d + D_n m_1 - s \end{vmatrix}, \tag{3d}$$

and

$$\Delta = \begin{pmatrix} v_d + D_n m_2 - s & v_d + D_n m_1 - s \\ (v_d + D_n m_2 + v_e)e^{m_2 W_A} & (v_d + D_n m_1 + v_e)e^{m_1 W_A} \end{pmatrix}. \tag{3e}$$

Here, τ is the minority lifetime and W_A is the absorber thickness.

In order to enhance both bandwidth and efficiency, we used a graded doping profile to induce an electric field in the absorber. For a constant field value, which corresponds to an exponentially decreasing doping profile, the field magnitude is

$$|E| = \frac{1}{W_A}\frac{k_B T}{q}\ln\left(\frac{N_{A,\max}}{N_{A,\min}}\right) \tag{4}$$

where $k_B T/q$ is the thermal voltage and N_A is the acceptor concentration. The field can be made larger by increasing the difference between the low-end and high-end doping. The high-end doping is limited to about $2\text{-}3\cdot10^{19}$ cm^{-3} by both the solubility of boron in germanium and the need to keep optical loss from free-carrier absorption less than the inter-band absorption. The low-end doping is limited to about $1\cdot10^{18}$ cm^{-3} by the electrical properties of the heterojunction. The threading defects that form at the Si/Ge interface due to the

This article has been accepted for publication in a future issue of this journal, but has not been fully edited. Content may change prior to final publication. Citation information: DOI 10.1109/JLT.2014.2310780, Journal of Lightwave Technology

lattice mismatch between the two materials are known to be acceptor-like. They pin the Fermi level at the heterojunction to about 0.06 eV above the valance band [12]. Because of this, the doping in that area must be at least $5\cdot10^{17}$ cm^{-3} to avoid an unwanted barrier. Due to the fixed values of low-end and high-end doping, the absorber electric field strength is a function of absorber thickness.

Fig. 2 shows the calculated collection efficiency as a function of absorber thickness for several values of back-surface recombination velocity. The electric field strength was calculated using (4). Here, the collection efficiency η_c is defined as

$$\eta_c(s) = \frac{J_n(W_A)}{J_n(W_A)\big|_{s=0}}, \quad (5)$$

or the ratio of the electron current at the absorber-collector interface given the assumed value of back surface recombination velocity (s) to the same current assuming zero back surface recombination. The relative values of the exit velocity (for electrons entering the collector) and back surface recombination velocity, along with the electric field, are the most important parameters in determining the collection efficiency. The exit velocity assumed here is the thermal velocity of electrons in germanium. Other simulation parameters are given in Table 1. As expected, increasing the field strength (by decreasing the absorber thickness) increases collection efficiency. Thus for high collection efficiency, thin absorbers are clearly preferable.

TABLE I
SIMULATION PARAMETERS

Symbol	Quantity	Value
n_{Ge}	Germanium refractive index	4.17
α_{Ge}	Germanium absorption coeff.	3000 cm^{-1}
n_{Si}	Silicon refractive index	3.47
n_{SiO2}	Silicon dioxide refractive index	1.47
μ_n	Electron mobility[a]	2000 cm^2/Vs
τ	Electron lifetime	10 ns
D_n	Diffusion coefficient[a]	52 cm^2/s
v_e	Exit velocity	$1\cdot10^7$ cm/s
$v_{n,Si}$	Saturated electron velocity in silicon (see [10])	$1.2\cdot10^7$ cm/s

[a] Electron mobility was calculated from [13] assuming a constant doping around $5\cdot10^{18}$ cm^{-3}. The diffusion coefficient was calculated from the mobility value and the Einstein relation (using Boltzmann statistics).

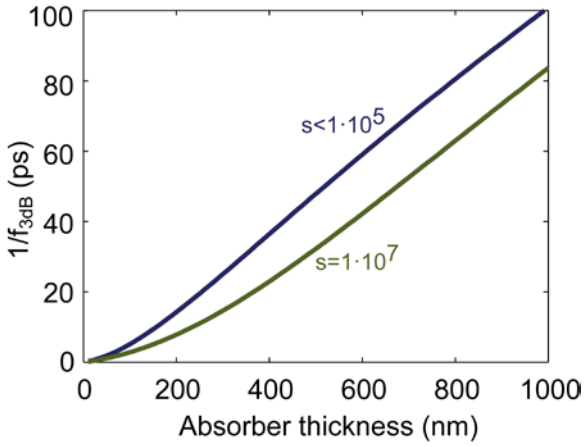

Fig. 3. Transit time as a function of absorber thickness for two different back surface recombination velocities calculated using (2)-(3). The electric field was assumed constant and calculated using (4). Other simulation parameters can be found in Table 1.

Equations 2-4 can also be used to solve for the frequency response of the device. Fig. 3 shows the inverse of the 3 dB frequency as a function of absorber thickness, calculated using the same assumptions and equations as above. For large back-surface recombination velocities, the frequency response is enhanced. This is because many of the electrons do not traverse the entire absorber (resulting in a decrease in collection efficiency evident in Fig. 2). To achieve operation above 40 GHz, regardless of back-surface recombination velocity, an absorber thinner than 400 nm must be used. Thus we used an absorber thickness of 175 nm, as it is the only germanium thickness that permits a short and efficient device and also lies below this cutoff value. Fig. 4 shows the simulated bandwidth as a function of both absorber and collector thicknesses, taking both transit time and R-C limits into account, for a 4 µm x 30 µm Si/Ge UTC photodiode. The diode capacitance was calculated using a parallel-plate model and assuming the depletion region thickness was equal to the collector thickness. Parasitic effects were not included. The final collector thickness was 400 nm, and was chosen to balance the transit time and the R-C limit.

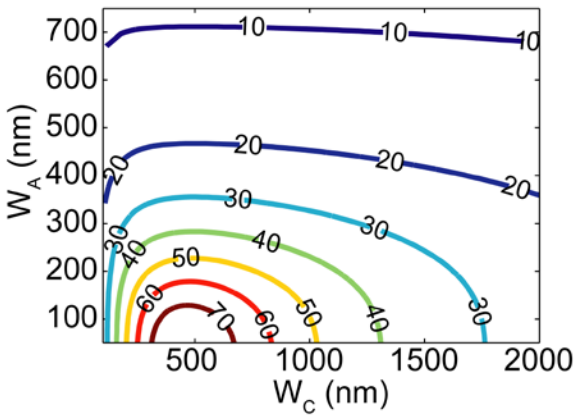

Fig. 4. Bandwidth contours (in GHz) for a 4 µm x 30 µm Si/Ge UTC photodiode. The simulation assumed a 50 Ω load and negligible parasitic capacitance and resistance.

III. FABRICATION

Fig. 5 shows the process used to fabricate waveguide Si/Ge UTC photodetectors. The n-well under the detector was patterned prior to growth. It was approximately 400 nm thick with a doping density of $1\cdot10^{18}$ cm^{-3} and a measured sheet resistance of 1.2 kΩ/□. The photodiode epitaxial layers were grown using selective area growth in wells much larger than the final photodiode dimensions. This allowed the detector mesas and input waveguide to be patterned in the same

This article has been accepted for publication in a future issue of this journal, but has not been fully edited. Content may change prior to final publication. Citation information: DOI 10.1109/JLT.2014.2310780, Journal of Lightwave Technology

lithography and etch step, avoiding the need for careful alignment between the two layers. Photodetector mesas and waveguides were formed using an inductively coupled plasma SF_6/O_2 etch. Because the photodiodes are taller than the silicon waveguides, this required two etch steps; the same Cr/ SiO_2 hard-mask was used for both.

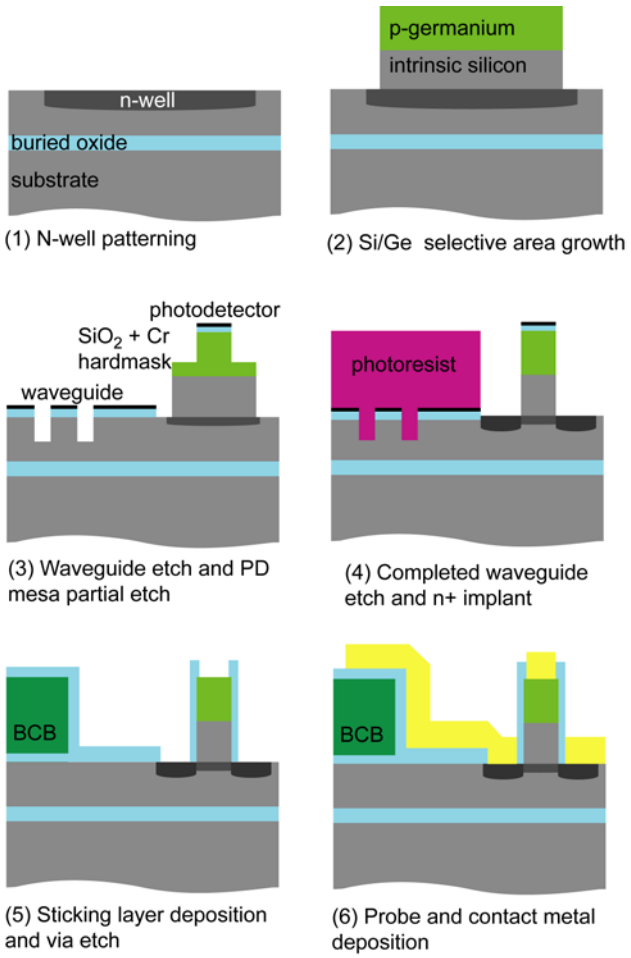

Fig. 5. Fabrication process used for Si/Ge UTC photodiodes.

After the waveguide and mesa etch, the n+ contacts were formed. The same Cr hard-mask used for the waveguide and mesa etch was used for this step, so that the n+ contact areas were self-aligned to the detector mesas. The contact doping density was approximately $1{\cdot}10^{20}$ cm^{-3}. The phosphorus implants were activated in a 5 minute 600 ºC anneal. Following the activation anneal, a 500 nm layer of PECVD SiO_2 was deposited everywhere and BCB was patterned under the probe pads. Then vias were etched in the SiO_2 and Ni/Ti/Au (30 nm/100 nm/1 µm) probe/contact metal was deposited.

IV. DC CHARACTERISTICS

Fig. 6 shows the reverse I-V characteristics of the 3 µm x 90 µm and the 4 µm x 13 µm devices considered in this work. Both devices were fabricated from the same epitaxial material and have the same absorber and collector thicknesses. The dark current at -1 V was 36 nA for the longer device and 24 nA for the shorter one. The dark currents of both devices are similar until around -2.5 V, at which voltage the 4 µm x 13 µm device dark current increases substantially. This was not typical; most detectors fabricated on the same wafer had reverse I-V curves more similar to the 3 µm x 90 µm device. It is most likely due to breakdown of the dielectric layer on the sidewall of the device. At -5 V, the dark current of the longer device was 700 nA and the dark current of the shorter detector was 20 µA. All dark current values were measured in a dark room at 25 ºC.

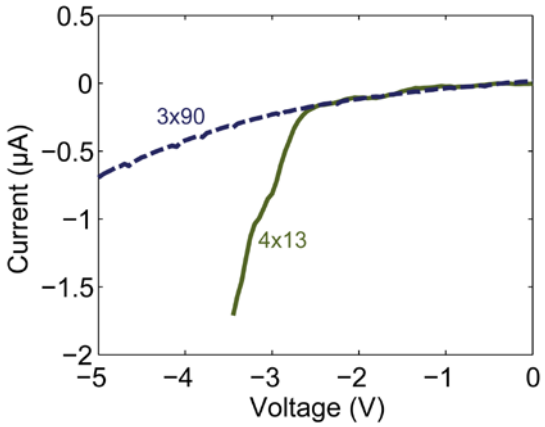

Fig. 6. Dark currents of the 3 µm x 90 µm and 4 µm x 13 µm devices.

Fig. 7 shows the responsivity of a 90 µm long device as a function of reverse bias at 1550 nm. Polarization was controlled during the experiment, and the polarization dependence was 1 dB. The 11 dB coupling loss between the waveguide and lensed fiber has been subtracted from the input optical power. The responsivity increases from 0.55 A/W at -1 V bias to 0.7 A/W at -5 V. This is most likely due to an increase in collection efficiency. As the voltage is increased, the electric field at the silicon/germanium interface also increases. The result is that more photogenerated electrons are collected by the external circuit rather than recombining at the

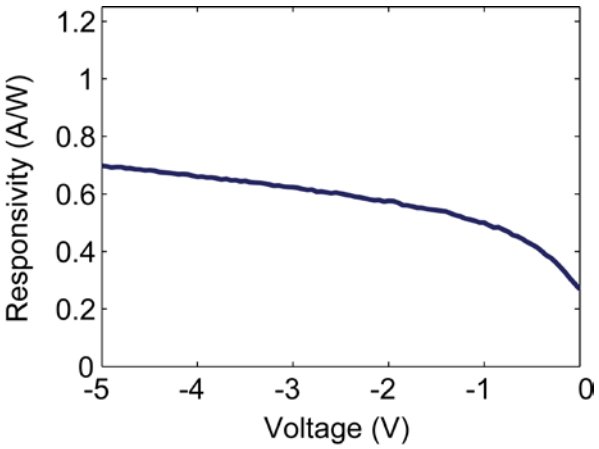

Fig. 7. Responsivity as a function of voltage for the 3 µm x 90 device.

p-contact. Since the expected electric field in the collector is well below the breakdown voltage of silicon, the increase in

This article has been accepted for publication in a future issue of this journal, but has not been fully edited. Content may change prior to final publication. Citation information: DOI 10.1109/JLT.2014.2310780, Journal of Lightwave Technology

responsivity is unlikely to be due to avalanche gain.

Fig. 8 shows the responsivities of several devices at 1550 nm and -1 V bias as a function of detector length. Polarization was again controlled during the experiment and chosen to optimize responsivity. The simulated curve (simulated using the method described in Section II) is also shown and agrees qualitatively with the data. The simulation predicts responsivity values about two times larger than the measured values; in order to facilitate qualitative comparison, the theory curve has been scaled to match the data. At least 1 dB of the discrepancy between theory and measurement is due to the voltage-dependence of the collection efficiency. The remaining 2 dB difference between simulation and experiment is most likely due to excess modal loss (e.g. metal loss) or waveguide propagation loss. The excess modal loss from the top metal contact and from free-carrier absorption in the n-silicon was not included in the simulation, which causes the simulation to over-estimate the efficiency. To calculate the optical power at the input of the device, we subtracted the measured facet coupling loss, but assumed that the loss of the 1 mm long input waveguide was negligible, which may not be the case. The expected loss for this type of waveguide is about 2 dB/cm, though it can be much higher if the waveguide is damaged during fabrication.

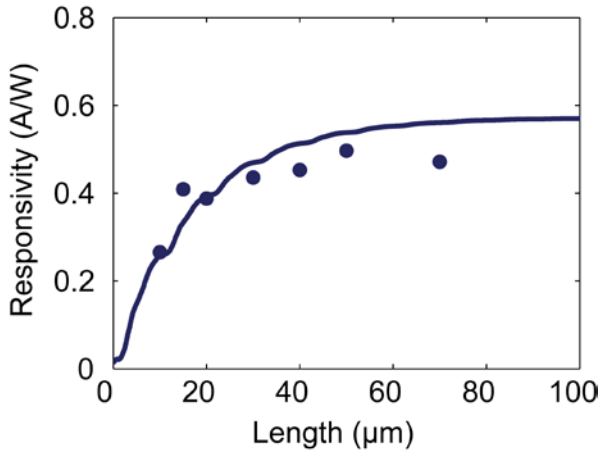

Fig. 8. Measured (dots) and simulated (line) responsivity as a function of device length at 1550 nm and -1 V bias. The simulation was done using the beam propagation method using material parameters given in Table 1. To enable a qualitative comparison, the simulated curve has been scaled to fit the data.

V. RF CHARACTERISTICS

Fig.s 9 and 10 show the extracted capacitance and series resistance for the Si/Ge UTCs from -2 to -5 V bias. The diode impedance (Z_{PD}) was extracted from the microwave reflection coefficient (S_{22}) using

$$S_{22} = \frac{Z_{PD} - Z_0}{Z_{PD} + Z_0} \tag{6}$$

where Z_0 is the system impedance, and diode capacitance and series resistance were found by fitting the data to the equivalent circuit model shown as an inset in Fig. 10. For small devices, which typically have large series resistances (relative to 50 Ω) and small capacitances (relative to the pad capacitance), using (6) directly accurately determines the total (detector plus pad) capacitance, but can result in a poor approximation of the series resistance. Thus to extract the values in Fig. 9 and Fig. 10 from the raw microwave reflection data, the pad impedance was calibrated out before resistance and capacitance values were fit.

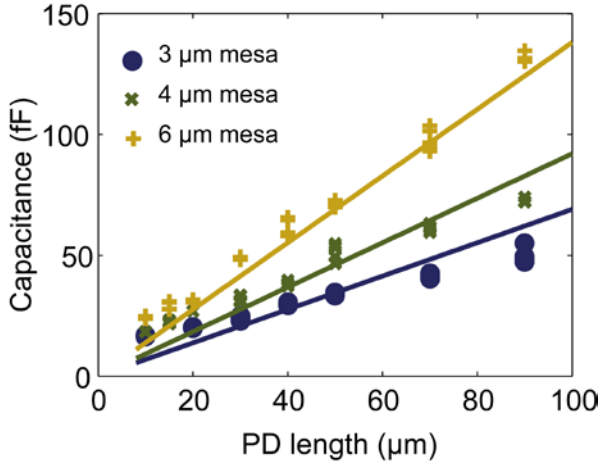

Fig. 9. Diode capacitance as a function of device length. The devices were biased at -2, -4, and -5 V (all shown on the same curve). The straight lines were fitted to the entire data set assuming a constant capacitance per unit area.

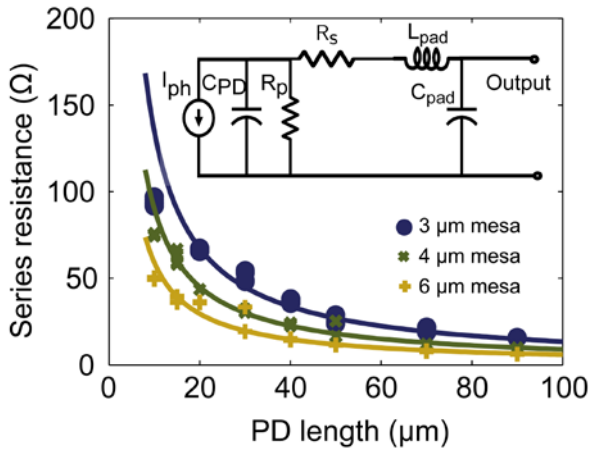

Fig. 10. Series resistance as a function of device length. The devices were biased at -2, -4, and -5 V (all shown together). The curves were fit to the entire data set. Inset: equivalent circuit model used to fit parameters to S_{22} data.

To estimate the pad capacitance, the small-circuit equivalents of many photodiodes with different dimensions were found, neglecting the effect of the pad capacitance. Then the pad capacitance was extracted by assuming a constant capacitance per unit area. Since neglecting the pad capacitance has a small impact on capacitance error, this is expected to be accurate. Corrected reflection coefficient values were generated using

This article has been accepted for publication in a future issue of this journal, but has not been fully edited. Content may change prior to final publication. Citation information: DOI 10.1109/JLT.2014.2310780, Journal of Lightwave Technology

$$S_{22,corr} = \frac{S_{22} - \frac{j\omega C_{pad} Z_0}{2 + j\omega C_{pad} Z_0}}{\left(\frac{2}{2 + j\omega C_{pad} Z_0}\right)^2 + \frac{-j\omega C_{pad} Z_0}{2 + j\omega C_{pad} Z_0}\left(S_{22} - \frac{-j\omega C_{pad} Z_0}{2 + j\omega C_{pad} Z_0}\right)} \quad (7)$$

where $S_{22,corr}$ is the corrected reflection coefficient, S_{22} is the measured reflection coefficient, and C_{pad} is the pad capacitance. The process was repeated until a self-consistent value (within 250 aF) for the pad capacitance was found. The pad capacitance estimated using this technique was 16 fF. This value agrees well with data from pad-only test structures with the same layout fabricated on similar substrates.

The measured diode capacitance is linearly proportional to area, and the slope of the line is as expected for photodiodes with areas larger than 200 μm^2: A simple parallel-plate model predicts 259 aF/μm^2 using the collector as the intrinsic region thickness, while the measured slope was 231 aF/μm^2. This corresponds to an additional thickness of depleted silicon of 50 nm, which is reasonable given the n-well doping. This straight line fit is shown in Fig. 9. The extracted capacitances of small photodiodes are typically larger than the straight-line fit. This is most likely due to the fringe capacitance, which is expected to be 1-2 fF for these devices [14], [15].

The series resistance shown in Fig. 10 appears to be dominated by the p-contact resistance, as narrower photodiodes have higher series resistances. The p-contact resistance, measured using cross-bridge Kelvin structures, was $1 \cdot 10^{-5}$ Ω·cm^2, which accounts for almost the full series resistance. For p-type germanium with this level of doping, much lower contact resistances have been demonstrated [16]. The poor contact resistance may be due to damage to the semiconductor prior to the contact metal deposition.

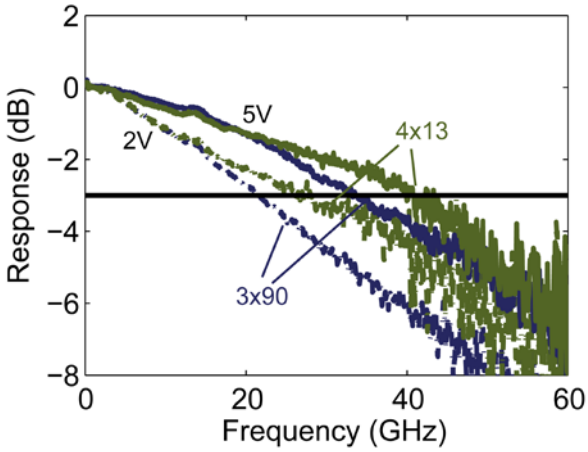

Fig. 11. Frequency responses of the two photodiodes at -2V and at -5V bias.

Fig. 11 shows the frequency responses of the 3 μm x 90 μm and the 4 μm x 13 μm devices at -2 V and -5 V bias. The frequency response was measured with an Agilent lightwave component analyzer at 1550 nm and includes the effect of the probe pad impedance, though the attenuation of the RF cable and probe was removed in the calibration process. At -5 V bias, the 3 dB electrical bandwidth of the 3 μm x 90 μm detector was 33 GHz while for the 4 μm x 13 μm detector, it was 40 GHz. The corresponding optical bandwidths (i.e. $10\log_{10}(S_{21})$) of the two devices are 54 GHz and 56 GHz, respectively.

Fig. 12 shows the R-C and transit-time contributions to the 3 μm x 90 μm Si/Ge UTC at -5 V bias. The R-C contribution was extracted from the S_{22} data using

$$S_{21} = 20\log_{10}\frac{|Z_{PD} - R_s|}{|Z_L + Z_{PD}|} \quad (8)$$

where the load impedance (Z_L) is 50 Ω and the series resistance was 27 Ω. The diode impedance Z_{PD} was taken using corrected S_{22} data from (7). The transit time response was calculated by dividing the total response by the extracted R-C response. The transit-time limited bandwidth extracted this way displayed a strong voltage dependence, but the R-C-limited bandwidth did not.

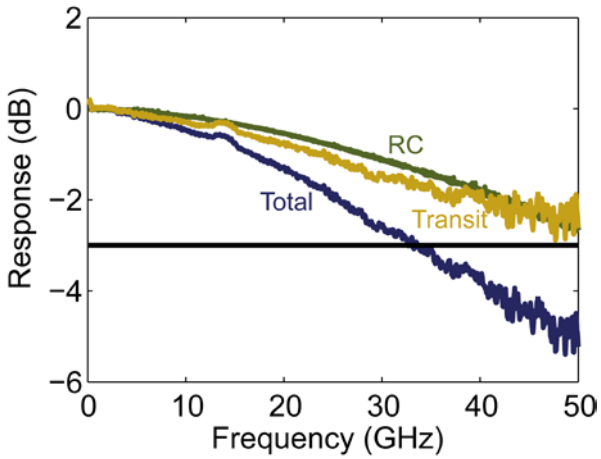

Fig. 12. Transit-time and R-C contributions to the frequency response of the 3 μm x 90 μm photodiode at -5V bias.

VI. Power Handling

The large-signal compression characteristics of the 40 GHz 4 μm x 13 μm and the 33 GHz 3 μm x 90 μm devices discussed above are shown in Fig. 13. An 80% modulation depth tone fixed at 30 GHz was generated using the standard heterodyne technique with two free-running lasers at 1537 nm. The RF power was measured on an electrical spectrum analyzer. The loss of the cables was measured with a network analyzer and subtracted from the data. In both cases, the -1 dB compression current is around 2 mA, which corresponds to an output power around -20 dBm. However, the longer device has larger maximum output power since the output power continues to increase after the -1 dB compression current is reached. This is because the back of the device continues to operate in the linear regime even when the front of the device is compressed, whereas for the shorter device, the current is more uniformly distributed. This leads to a sharp decrease in output power beyond the -1 dB compression current for the shorter device, in contrast to a slow increase in output power

This article has been accepted for publication in a future issue of this journal, but has not been fully edited. Content may change prior to final publication. Citation information: DOI 10.1109/JLT.2014.2310780, Journal of Lightwave Technology

for the longer one. The maximum output power of the 4 µm x 13 µm detector is -21.4 dBm, while it is -11.7 dBm for the longer one.

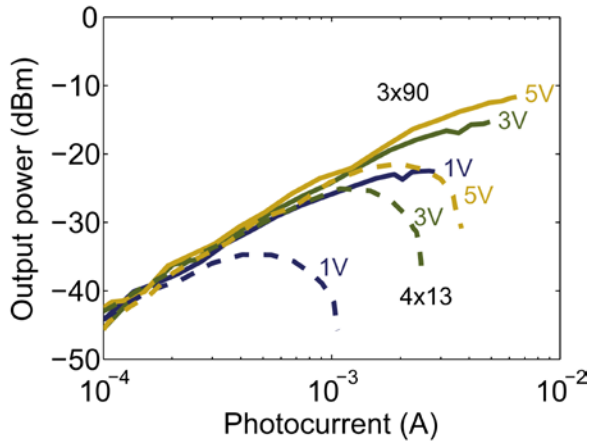

Fig. 13. Output power as a function of photocurrent for both photodiodes for a large-signal input at 30 GHz.

Fig. 14 shows the -1 dB compression current as a function of bias voltage for both devices at different operating frequencies. Using the waveguide photodiode nonlinearity simulation technique discussed in [17], we simulated the expected space-charge limited -1 dB compression current as a function of bias voltage. For a space-charge limited 3 µm x 90 µm device with this cross-section and absorption profile, the expected slope of the line shown in Fig. 14 is 4 mA/V. Instead, the measured slope id 0.4 mA/V, implying that the voltage-dependence of the bandwidth evident in Fig. 11, rather than the space-charge effect, is responsible for compression. These results indicate that the most effective way to improve the compression characteristics of the devices will be to decrease the voltage dependence of the bandwidth. This can most likely be achieved through more careful band-engineering of the heterojunction.

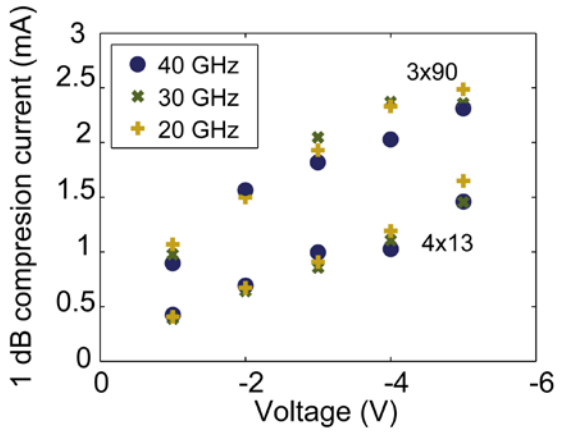

Fig. 14. 1 dB compression current for both photodiodes as a function of bias voltage at 20 GHz, 30 GHz, and 40 GHz.

VII. Conclusion

We have demonstrated and developed the theory of waveguide-coupled Si/Ge uni-traveling carrier photodiodes. The UTC structure decouples the germanium thickness from the intrinsic region thickness, which enables independent optimization of the absorption profile and power-handling capability. The fabricated photodiodes showed good responsivity, bandwidth, and power-handling. Optimization of the Si/Ge interface is expected to yield further improvement in all three metrics.

Acknowledgment

Epitaxial growth was done by Lawrence Semiconductor Research Laboratories. Fabrication made use of the UCSB nanofab. We would like to thank Anand Ramaswamy, Jin-Wei Shi, Joe Campbell, and Andreas Beling for useful discussions.

References

[1] D. Guckenberger, "Microwave photonic applications for silicon photonics," in *Proc. OFC*, San Diego, CA, 2009 paper OWS1.

[2] G. Fish, "Heterogeneous photonic integration for microwave photonic applications," in *Proc. OFC*, Anaheim, CA, 2013, paper OW3D.5.

[3] J. Cardenas, P. Morton, J. Khurgin, A. Griffith, C. Poitras, K. Preston, and M. Lipson, "Linearized silicon modulator based on a ring assisted Mach Zehnder inteferometer," *Opt. Express* vol. 21, no. 19, pp. 22549-22557, Sept. 2013.

[4] L. Vivien, A. Polzer, D. Marris-Morini, J. Osmond, J. M. Hartmann, P. Crozat, E. Cassan, C. Kopp, H. Zimmermann, and J. M. Fédéli, "Zero-bias 40Gbit/s germanium waveguide photodetector on silicon," *Opt. Express*, vol. 20, no. 2, pp. 1096–1101, Jan. 2012.

[5] A. Ramaswamy, M. Piels, N. Nunoya, T. Yin, and J. E. Bowers, "High power silicon-germanium photodiodes for microwave photonic applications," *IEEE Trans. Microw. Theory Tech.*, vol. 58, no. 11, pp. 3336–3343, Nov. 2010.

[6] J. E. Bowers and C. Burrus, "Ultrawide-band long-wavelength p-i-n photodetectors," *J. Lightw. Tech.*, vol. LT-5, no. 10, pp. 1339–1350, Oct. 1987.

[7] J. Michel, J. Liu, and L. C. Kimerling, "High-performance Ge-on-Si photodetectors," *Nat. Photon.*, vol. 4, no. 8, pp. 527–534, Jul. 2010.

[8] K. S. Giboney, M. J. W. Rodwell, and J. E. Bowers, "Traveling wave photodetector design and measurements," *IEEE J. Sel. Topics Quantum Electron.*, vol. 2, no. 9, pp. 622–629, Sep. 1996.

[9] K. Williams and R. Esman, "Design Considerations for High-Current Photodetectors," *J. Lightw. Tech.*, vol. 17, no. 8, pp. 1443-1454, Aug. 1999.

[10] M. Piels and J. E. Bowers, "Si/Ge uni-traveling carrier photodetector," *Opt. Express*, vol. 20, no.7, pp. 7488-7495, Mar. 2012.

[11] T. Ishibashi, S. Kodama, N. Shimizu, and T. Furuta, "High-speed response of uni-traveling-carrier photodiodes," *Jpn. J. Appl. Phys.*, vol. 36, no. 10, pp. 6263–6268, Oct. 1997.

[12] C. Claeys and E. Simoen, "Electrical and optical properties," in *Fundamental and Technological Aspects of Extended Defects in Germanium*, ser. Springer Series in Materials Science. Springer Berlin Heidelberg, 2009, vol. 118, pp. 65–136.

[13] S. Adachi, *Handbook on Physical Properties of Semiconductors*. Springer-Verlag, 2004, vol. 1.

[14] W. Chang, "Analytical IC metal-line capacitance formulas," *IEEE Trans. Microw. Theory Tech.*, vol. 24, no. 9, pp. 608 – 611, Sep. 1976.

[15] ——, "Correction to analytical IC metal-line capacitance formula," *IEEE Trans. Microw. Theory Tech.*, vol. 25, no. 8, p. 712, Aug. 1977.

[16] D. P. Brunco, B. De Jaeger, G. Eneman, J. Mitard, G. Hellings, A. Satta, V. Terzieva, L. Souriau, F. E. Leys, G. Pourtois, M. Houssa, G. Winderickx, E. Vrancken, S. Sioncke, K. Opsomer, G. Nicholas, M. Caymax, A. Stesmans, J. Van Steenbergen, P. W. Mertens, M. Meuris, and M. M. Heyns, "Germanium MOSFET devices: Advances in materials understanding, process development, and electrical performance," *Journal of The Electrochemical Society*, vol. 155, no. 7, pp. H552-H561, May 2008.

[17] M. Piels, A. Ramaswamy, and J. E. Bowers, "Nonlinear modeling of waveguide photodetectors," *Opt. Express*, vol. 21, no. 13, pp. 15634–15644, Jul. 2013.